An Operational Land Surface Temperature Retrieval Methodology for Chinese Second-Generation Huanjing Disaster Monitoring Satellite Data

Enyu Zhao , Caixia Gao , Qijin Han, Yuying Yao, Yulei Wang, *Member, IEEE*, Chunyan Yu, *Member, IEEE*, and Haoyang Yu, *Member, IEEE*

Abstract—The Chinese second-generation Huanjing disaster monitoring satellite (HJ-2A) was launched on September 27, 2020, and underutilized due to the lack of accurate operational methodologies for land surface temperature (LST) retrieval. In this article, an operational LST retrieval method is proposed to retrieve LSTs from HJ-2A thermal infrared observations. The LST retrieval methodology involves two main steps. The land surface emissivities (LSEs) over all land cover types are obtained with the improved normalized difference vegetation index-based threshold method, and then the LST is retrieved operationally from the adjacent infrared bands. The algorithm coefficients for LST retrieval are from regression analysis of radiative transfer simulations, and LSTs could be retrieved based on thermal images without any additional auxiliary data. The simulation results demonstrated that the root-mean-square errors (RMSEs) of LST retrieval were less than 2.4 K in all subranges, and the minimum RMSE for the two emissivity groups (high- (low-) emissivity group) was 0.16 K (0.20 K) and appeared in the tractable subrange with water vapor content (WVC) varying from 0 to 1.5 g/cm^2 and view zenith angle (VZA) being 0°. Furthermore, an error analysis was performed, the results showed that the LSE, NEΔT, and atmospheric water vapor uncertainty of 1%, 0.2 K, and 20% caused the LST retrieval errors with 0.88–1.21 K (0.84–1.19 K), 0.1 K (0.09 K), and 0.006 K (0.008 K) for the high- (low-) emissivity group, respectively, with WVC$\in$[0–1.5] g/cm^2 and VZA = 0°. Finally, the retrieved LSTs were applied to seven images of the Wuhai, Geermu, Dunhuang, and Baotou sites from January to March and cross validated by the moderate resolution imaging spectroradiometer (MODIS) LST products. From the cross-validated results, it can be found that the RMSEs of the retrieved LSTs and the MODIS LST products were between 2.3 and 3.7 K, and the mean RMSE value was 2.89 K.

Index Terms—Generalized split-window (GSW) algorithm, HJ-2A/IRS satellite, land surface emissivity (LSE), land surface temperature (LST), thermal infrared (TIR).

I. Introduction

LAND surface temperature (LST) is an important indicator of the energy equilibrium of the Earth's surface and a critical parameter in the physical processes of surface energy from local to global scales. Moreover, many applications, such as greenhouse effect monitoring, urban climate monitoring, vegetation monitoring, drought monitoring, surface soil moisture estimation, meteorological studies, biogeochemical studies, and environmental studies, rely on LST knowledge [1]–[8]. With the development of aerospace technology, infrared satellites, such as moderate resolution imaging spectroradiometer (MODIS), Gaofen-5, advanced spaceborne thermal emission and reflection radiometer, Chinese second-generation Huanjing disaster monitoring satellite (HJ-2A), and the spinning enhanced visible and infrared imager, provide us with the only reliable global observation data available from which LSTs can be obtained [9]–[15].

To date, the LSTs can be retrieved using the proposed algorithms based on the thermal infrared (TIR) observations [16]–[25]. These retrieval methods can be divided into three categories according to different emphases: multichannel methods, single-channel methods, and multiangle methods. Among these methods, an algorithm called the split-window (SW) algorithm belonging to the multichannel method is the most widely used to obtain LSTs [26]–[28]. McMillin [29] first proposed the SW method to retrieve the sea surface temperatures (SSTs) in the absence of any previous atmospheric information. Due to the excellent performance of the SW algorithm in SST retrieval, scientists adapted the SW algorithm in order to retrieve LSTs. In 1996, by analyzing the difference of atmospheric absorption characteristics in adjacent TIR channels, Wan and Dozier [30] expressed the surface temperatures as a linear function of brightness temperatures to retrieve the LSTs. Wan [31] added a term of the quadratic difference between the two adjacent TIR brightness temperatures to the generalized split-window (GSW) algorithm to improve the LST retrieval accuracy.

The HJ-2A satellite was successfully launched on September 27, 2020, which provides the infrared multispectral scanner

Enyu Zhao, Yuying Yao, Yulei Wang, Chunyan Yu, and Haoyang Yu are with the Information Science and Technology College, Dalian Maritime University, Dalian 116026, China (e-mail: zhaoenyu@dlmu.edu.cn; yyy_161121@163.com; wangyulei@dlmu.edu.cn; yuchunyan1997@126.com; yuhy@dlmu.edu.cn).

Caixia Gao is with the Key Laboratory of Quantitative Remote Sensing Information Technology, Aerospace Information Research Institute, Chinese Academy of Sciences, Beijing 100094, China (e-mail: gaocaixia@aoe.ac.cn).

Qijin Han is with the China Center for Resources Satellite Data and Application, Beijing 100094, China (e-mail: hanqijin@chinasiwei.com).

(IRS) payload, including two TIR channels and two midinfrared channels with a spatial resolution of 96 m and a swath width of 720 km to collect the surface thermal emission information. The noise-equivalent temperature difference is 0.2 K for both of the two TIR channels, and bandwidth is from 10.5 to 11.4 μm and from 11.5 to 12.5 μm, respectively. The successful launch of HJ-2A greatly improves China's ability to acquire the visible, infrared, and hyperspectral data and meets the urgent need for a continuous supply of remote sensing data in related fields. HJ-2A will play an important role in environmental monitoring and ecological protection in the future. However, until now, there has been no report of retrieving LSTs from HJ-2A/IRS satellite TIR data.

The aim of this article is to provide a proposed operational LST retrieval method to retrieve LSTs from HJ-2A/IRS TIR observations and LSTs could be retrieved based on thermal images without any additional auxiliary data. The LST retrieval methodology involves two main steps. The land surface emissivities (LSEs) over all land cover types are obtained with the improved normalized difference vegetation index (NDVI) based threshold method, and then the LST is retrieved operationally from the two adjacent infrared bands for correcting the atmospheric effects due to their different absorptions.

The rest of this article is organized as follows. Sections II and III describe the data simulation and the methodology, respectively. The results and sensitivity analysis [the uncertainty in the instrument noise, the LSE, and water vapor content (WVC)] of the simulated data are presented in Section IV. Section V provides the preliminary application to HJ-2A/IRS data. Finally, Section VI concludes this article.

II. DATA SIMULATION

In the study, the simulated HJ-2/IRS data under different atmosphere and surface conditions are generated for calculating the coefficients of LST retrieval algorithm on the basis of the radiative transfer theory. The thermodynamic initial guess retrieval (TIGR) atmosphere profile data and the emissivity library developed by MODIS University of California at Santa Barbara (UCSB) are used for the simulation. For the given LSTs, the top of the atmosphere (TOA) radiances under view zenith angle (VZA) of 0°–60° are simulated with the aid of moderate-spectral resolution atmospheric transmittance model (MODTRAN).

A. Atmospheric Profile Data

The TIGR dataset, which contains 2311 representative atmospheric profiles from tropical to polar with WVCs ranging from 0.1 to 7 g/cm^2, is used to develop the LST retrieval algorithm [32]. Each of the TIGR atmospheric profiles is described by the temperature, water vapor, and ozone concentration values on a given pressure grid from the surface to the TOA. Since the LST retrieval only considers the conditions of clear sky, a total of 884 atmospheric profiles are selected from the TIGR dataset, with the WVC values ranging from 0.0614 to 6.2687 g/cm^2 and the atmospheric bottom temperature (T_a) values varying from 240.05 to 314.16 K, as shown in Fig. 1.
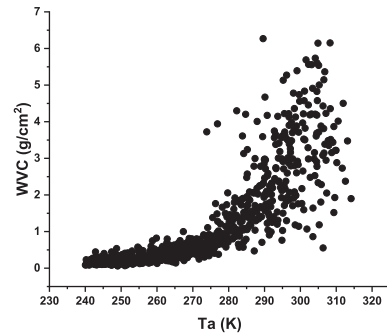

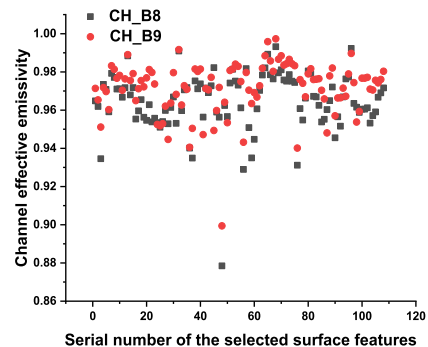Fig. 1.   Relationship between the WVC and T_a of the selected atmospheric files.

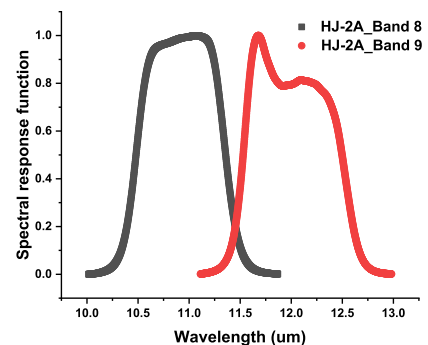Fig. 2.   Channel LSEs of the HJ-2A/IRS TIR channels.

Fig. 3.   Spectral response functions of HJ-2A/IRS TIR channels.

B. LSE Data

The UCSB emissivity library contains the absolute emissivity spectra of vegetation, man-made material, soil, mineral, water, ice, and snow with wavelengths ranging from 3.0 to 14.5 μm. In total, 108 emissivity spectra of surface features, including 70 soil/mineral types, 28 vegetation types, and 10 man-made material types, are chosen from the UCSB library for the simulation. Some surface features with relatively lower emissivities are selected in order to simulate the real LST retrieval situations. The effective LSEs of HJ-2A/IRS TIR channels, which are calculated by (2), are displayed in Fig. 2. The spectral response functions of the HJ-2A/IRS TIR channels are shown in Fig. 3. The emissivity values vary from 0.8614 to 0.9932 for HJ-2A/IRS band 8 (CH_B8) and from 0.8994 to 0.9973 for HJ-2A/IRS band 9 (CH_B9).

C. Simulated HJ-2A Data

According to the radiative transfer theory, the solar radiation at 8–14 μm can be ignored for the tiny contribution, then the TOA radiances for the cloud-free atmospheres can be expressed as follows [33]:

$$B_\lambda(T_\lambda) = \tau_\lambda[\varepsilon_\lambda B_\lambda(T_s) + (1 - \varepsilon_\lambda)R_{at\_\lambda\downarrow}] + R_{at\_\lambda\uparrow} \quad (1)$$

where $B_\lambda(T)$ is the TOA radiance at wavelength λ, T is the blackbody temperature, T_λ is the TOA brightness temperature at wavelength λ, τ_λ is the transmittance at wavelength λ, $R_{at\_\lambda\downarrow}$ and $R_{at\_\lambda\uparrow}$ are the downward and upward radiances at wavelength λ, respectively, ε_λ is the emissivity at wavelength λ, and T_s is the surface temperature.

Considering that the radiances measured by most multichannel satellite sensors are in a finite spectral bandwidth, the channel quantities can be expressed as follows [34]:

$$X_i = \frac{\int_{\lambda_1}^{\lambda_2} f_i(\lambda)X_\lambda d\lambda}{\int_{\lambda_1}^{\lambda_2} f_i(\lambda)d\lambda} \quad (2)$$

where λ_1 and λ_2 are the lower and upper boundaries of the channel, respectively, $f_i(\lambda)$ is the spectral response function of HJ-2A/IRS TIR channel (see Fig. 3), and X is $B(T)$, τ, ε, $R_{at\downarrow}$, and $R_{at\uparrow}$.

The MODTRAN 5.0 is used to simulate the atmospheric parameters, including τ_λ, $R_{at\_\lambda\downarrow}$, and $R_{at\_\lambda\uparrow}$. Then, the channel effect atmospheric parameters can be calculated with the HJ-2A/IRS spectral response function by (2). The LST is set to be $T_a - 5$ K to $T_a + 15$ K with a step of 5 K in order to make the simulated data closer to the real observation situations [35]–[37]. The secant value of the VZA is set to be 1, 1.2, 1.4, 1.6, 1.8, and 2.0, respectively, with a step of 0.2.

For the given LSTs with atmospheric parameters and effective emissivities, the TOA radiances can be determined by (1) and (2). In total, 2 864 160 different situations (884 atmospheric profiles × 5 LSTs × 108 LSEs × 6 VZAs) are simulated for the LST retrieval algorithm.

III. METHODOLOGY

A. LST Retrieval Algorithm

Wan [31] added a quadratic difference term between two adjacent TIR brightness temperatures based on the GSW algorithm to retrieve LSTs from MODIS data, expressed as follows:

$$\begin{aligned} T_s = a_0 &+ (a_1 + a_2\frac{1-\varepsilon}{\varepsilon} + a_3\frac{\Delta\varepsilon}{\varepsilon^2})\frac{T_i+T_j}{2} \\ &+ (a_4 + a_5\frac{1-\varepsilon}{\varepsilon} + a_6\frac{\Delta\varepsilon}{\varepsilon^2})\frac{T_i-T_j}{2} + a_7(T_i - T_j)^2 \end{aligned} \quad (3)$$

where ε_i and ε_j are the LSEs in the two TIR channels, ε is the averaged emissivity with $\varepsilon = (\varepsilon_i + \varepsilon_j)/2$, $\Delta\varepsilon$ is the emissivity difference between the two TIR channels with $\Delta\varepsilon = \varepsilon_i - \varepsilon_j$, T_i and T_j are the brightness temperatures measured at the TOA, and a_0–a_7 are the unknown coefficients that can be calculated from the simulated data.

To improve the accuracy of LST inversion, the WVC and average emissivity are divided into several subranges in advance. The WVCs are set to be [0, 1.5], [1, 2.5], [2, 3.5], [3, 4.5],

[4, 5.5], and [5, 6.5] g/cm². Then, the averaged emissivity ε is divided into two groups according to the value of the averaged emissivity: One group has an averaged emissivity less than 0.97 and is called the low-emissivity group with 56 emissivity files; the other has an averaged emissivity larger than 0.97 and is called the high-emissivity group with 52 emissivity files.

B. LSE Retrieval Algorithm

From (1), it can be seen that the values of surface temperature and surface emissivity are coupled together because of TIR radiative transmission, and it is tough to separate them [38]. In this algorithm, the LSEs over all land cover types are retrieved by the improved NDVI-based threshold method [39]. In this algorithm, the image pixels are grouped into three categories according to the NDVI value. The pixel is classified as a bare soil pixel whose TIR emissivity can be obtained using (4) when the value of NDVI is less than 0.2; when the value of NDVI is larger than 0.5, the pixel is identified as the full vegetation pixel whose TIR emissivity can be obtained using (5); and when the value of NDVI varies from 0.2 to 0.5, the pixel is considered as a mixed pixel whose TIR emissivity can be calculated from (6), as follows:

$$\varepsilon_{si} = k_{i0} + \sum_{j=1}^{n} k_{ij}\rho_j \quad (4)$$

$$\varepsilon_{vi} = b_{i0} + \text{NDVI}_v \quad (5)$$

$$\varepsilon_i = \varepsilon_{vi}P_v + \varepsilon_{si}(1 - P_v) + C_i \quad (6)$$

where k_{i0} and k_{ij} are the regression coefficients, ε_{si} is the bare soil effective emissivity, n represents that there are n channels in the visible/near-infrared spectrum, ρ_j is the reflectance of channel j, ε_{vi} means the emissivity of the pixel that is regarded as the full vegetation pixel, b_{i0} is the fit coefficient, and ε_i represents the LSE value of the mixed pixel.

Using the following form, the vegetation proportion (P_v) can be obtained [40] as:

$$P_v = \left[\frac{\text{NDVI} - \text{NDVI}_s}{\text{NDVI}_v - \text{NDVI}_s}\right]^2 \quad (7)$$

where NDVI_v is the NDVI value for the pixel, which is regarded as the full vegetation pixel, and NDVI_s is the NDVI value for the pixel, which is considered as the bare soil pixel, and are set to be 0.5 and 0.2, respectively [41]. From the red and near-infrared reflectances, the NDVI value can be calculated.

In (6), the term C_i can be expressed as follows:

$$C_i = (1 - \varepsilon_{si})(1 - P_v)F\varepsilon_{vi} \quad (8)$$

where F ranges from 0 to 1, which is set to be 0.55.

IV. LST RETRIEVAL RESULT AND SENSITIVITY ANALYSES WITH SIMULATED DATA

In practice, LST retrieval from satellite observations requires two steps. First, the coefficients in (3) should be obtained from the simulated data; then, according to the WVC and emissivity
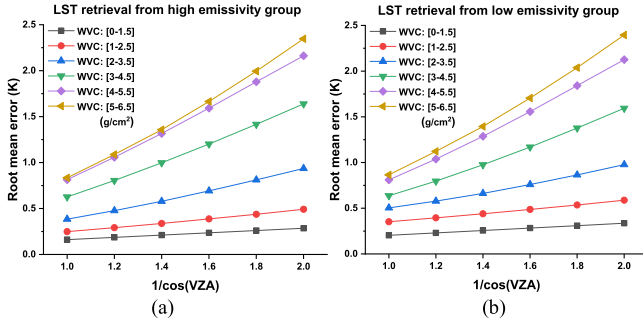
Fig. 4. LST retrieval RMSEs in tractable subranges. (a) For LST retrieval from high-emissivity group. (b) For LST retrieval from low-emissivity group.
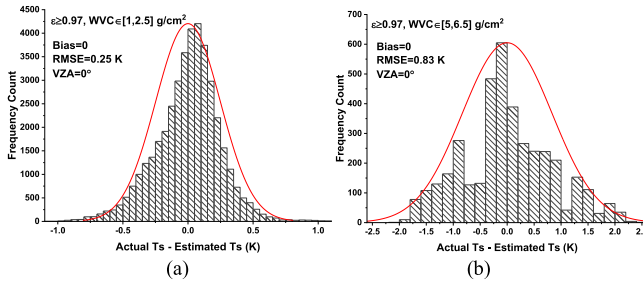

Fig. 5. Histogram of LST residual from the refined GSW algorithm with the envelope line for the high-emissivity group. (a) For WVC∈[1–2.5] g/cm^2 and VZA = 0°. (b) For WVC∈[5–6.5] g/cm^2 and VZA = 0°.

known in advance from the real satellite observations, the LST retrieval coefficients for tractable subranges can be selected.

A. Results of LST Retrieval With Simulated Data

The root-mean-square errors (RMSEs) of the LST retrievals for the two high- and low-emissivity groups are shown in Fig. 4. It can be seen that the RMSEs are less than 2.4 K in all subranges and it is apparent that the RMSEs increase as the WVCs and VZAs increase. Moreover, the LST retrieval accuracies of the high-emissivity groups are higher than those of the low-emissivity groups. The minimum RMSE for the high-emissivity group (low-emissivity group) is 0.16 K (0.20 K) with WVC belonging to [0–1.5] g/cm^2, and VZA = 0°, while the maximum RMSE for the high-emissivity group (low-emissivity group) is 2.35 K (2.40 K) in the highest WVC and largest VZA subrange.

For example, the differences between the true T_s and the estimated T_s obtained from the high-emissivity group using the coefficients for the subranges WVC∈[1–2.5] g/cm^2, VZA = 0° and WVC∈[5–6.5] g/cm^2, VZA = 60°, respectively, are shown in Fig. 5. As shown in this figure, the retrieval RMSE is 0.25 K under the dry atmospheric conditions and 0.83 K under the wet atmospheric conditions. Moreover, the maximum differences are ±1 K and ±2.5 K for the dry and wet atmospheric conditions, respectively. In the other WVC subranges, similar results can be obtained.

Fig. 6 displays the LST residual for the low-emissivity group using the coefficients for the subranges with WVC∈[1–2.5] g/cm^2, VZA = 0°, and with WVC∈[5–6.5] g/cm^2,
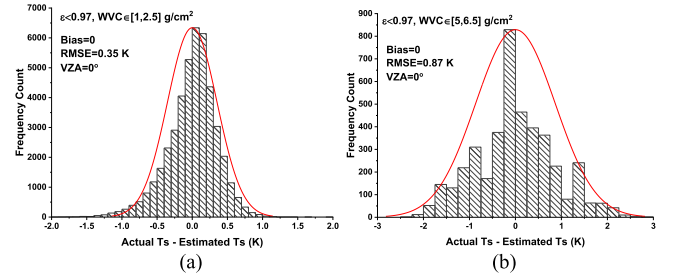

Fig. 6. Histogram of LST residual with the envelope line for the lower emissivity conditions. (a) For WVC∈[1–2.5] g/cm^2 and VZA = 0°. (b) For WVC∈[5–6.5] g/cm^2 and VZA = 0°.
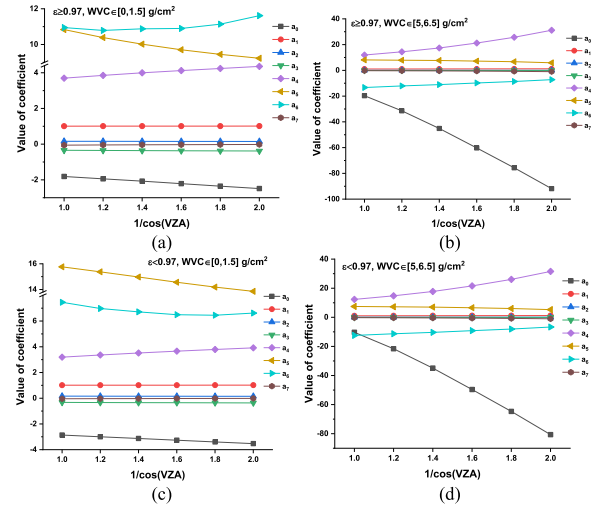

Fig. 7. Coefficients of refined GSW method. (a) For the subrange of high-emissivity group with WVC∈[0–1.5] g/cm^2. (b) For the subrange of high-emissivity group with WVC∈[5–6.5] g/cm^2. (c) For the subrange of low-emissivity group with WVC∈[0–1.5] g/cm^2. (d) For the subrange of low-emissivity group with WVC∈[5–6.5] g/cm^2.

VZA = 60°, respectively. In Fig. 6, the RMSE is 0.35 K for the dry atmospheric profiles and 0.87 K for the wet atmospheric profiles. Moreover, the maximum differences are ±1.5 K and ±3.0 K under dry and wet atmospheric conditions, respectively. In the other WVC subranges, similar results can be obtained.

The coefficients of the refined GSW are displayed in Fig. 7 as the functions of 1/VZA for the subrange with WVC belonging to [0–1.5] and [5–6.5] g/cm^2 for the two emissivity groups. As displayed in these figures, the fitting coefficients a_0–a_7 in (3) can be linearly expressed as a function of 1/VZA for the two emissivity groups.

B. Sensitivity Analysis

Instrument noise (noise-equivalent difference temperature, NEΔT), the uncertainty of the surface emissivity, and WVC are the three factors that mainly affect the accuracies of LST retrievals. Therefore, in this section, the three uncertainties are investigated.

1) Sensitivity Analysis of the NEΔT: Table I lists the RMSEs difference between the RMSEs without NEΔT and the RMSEs with NEΔT of 0.2 K (which is set according to the real instrument noise of HJ-2A/IRS) for the subranges of VZA = 0° in the

TABLE I
LST RETRIEVAL ERRORS CAUSED BY NEΔT FOR THE SUBRANGES VZA $= 0°$ IN HIGH- AND LOW-EMISSIVITY GROUPS WITH DIFFERENT WVCs

WVC (g/cm^2)	High-emissivity group			Low-emissivity group		
	NEΔT = 0 K	NEΔT = 0.2 K	Difference to NEΔT = 0 K	NEΔT = 0 K	NEΔT = 0.2 K	Difference to NEΔT = 0 K
[0,1.5]	0.16	0.26	0.10	0.20	0.29	0.09
[1,2.5]	0.19	0.28	0.09	0.23	0.31	0.08
[2,3.5]	0.21	0.29	0.08	0.26	0.33	0.07
[3,4.5]	0.24	0.31	0.07	0.28	0.35	0.07
[4,5.5]	0.26	0.33	0.07	0.31	0.37	0.06
[5,6.5]	0.29	0.35	0.06	0.34	0.39	0.05

TABLE II
STATISTICS OF THE ERRORS DUE TO THE UNCERTAINTY OF LSEs

Subrange	Conditions	α	β
WVC $\in$ [0–1.5] g/cm^2	High emissivity group, VZA=0°	[32.39,65.24]	[-110.89,-77.89]
	Low emissivity group, VZA=0°	[27.11,82.02]	[-105.47,-70.38]
WVC $\in$ [5–6.5] g/cm^2	High emissivity group, VZA=0°	[14.01,38.04]	[-51.96,-12.78]
	Low emissivity group, VZA=0°	[12.11,35.05]	[-51.29,-13.15]

Fig. 8. Overall error LST retrieval for the high- (low-) emissivity group with the uncertainties of NEΔT: 0.2 K, LSE: 1%, and WVC: 20%.

two emissivity groups with different WVCs. The influence of NEΔT on LST retrievals from small WVC conditions is larger than that from large WVC conditions. For the same atmospheric conditions, the influence of the NEΔT on LST retrieval from the high-emissivity group is almost the same as that from the low-emissivity group. When the NEΔT is 0.2 K, the maximum RMSE difference between the RMSE with NEΔT and RMSE without NEΔT is 0.10 K (0.09 K) when WVC varies from 0 to 1.5 g/cm^2 and VZA equals 0° in the high- (low-) emissivity groups.

2) Sensitivity Analysis of the Uncertainty of LSE: According to (3), the uncertainty of LSEs is dependent on the terms $(1-\varepsilon)/\varepsilon$ and $\Delta\varepsilon/\varepsilon^2$, and it can be expressed as follows:
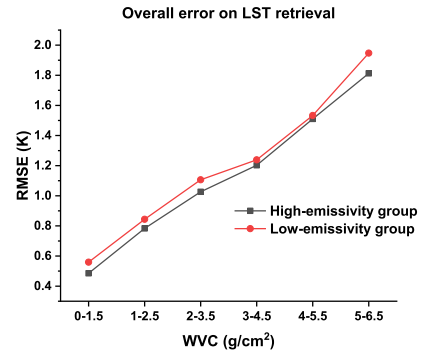
$$\alpha = a_2 \frac{T_i + T_j}{2} + a_5 \frac{T_i - T_j}{2} \qquad (9)$$

$$\beta = a_3 \frac{T_i + T_j}{2} + a_6 \frac{T_i - T_j}{2}. \qquad (10)$$

Therefore, the LST inversion errors caused by the uncertainty of LSE can be written as follows:

$$\delta\text{LST}_\varepsilon = \sqrt{\alpha^2\delta^2((1-\varepsilon)/\varepsilon) + \beta^2\delta^2(\Delta\varepsilon/\varepsilon^2)}. \qquad (11)$$

Table II lists the value ranges of α and β under dry atmospheres and wet atmospheres when the VZA is equal to 0° for the high- and low-emissivity groups. One can find that the α and β values obtained in the low-emissivity group are slightly smaller than that in the high-emissivity group in the same WVC subrange. For the same emissivity group, the values of α and β for the dry atmospheres are almost two times larger than those for the wet atmospheric conditions. The uncertainties of $(1-\varepsilon)/\varepsilon$ and $\Delta\varepsilon/\varepsilon^2$ are set to be 1%, for the high-emissivity group; the LST inversion errors are [0.88, 1.21] K for the dry atmospheres and [0.19, 0.64] K for the wet atmospheric conditions [42], [43]. For the low-emissivity group, the LST retrieval errors are [0.84,

1.19] K for the dry atmospheric conditions and [0.18, 0.62] K for the wet atmospheres.

3) Sensitivity Analysis of the Uncertainty of WVC: Table III lists the differences between the LST retrieval RMSEs with 20% uncertainty of WVC and LST retrieval RMSEs without WVC error for high- and low-emissivity groups [44], [45]. The influence of the WVC error increases as the WVCs and VZAs increase for both groups. The influence of the WVC error on the LST retrieval from the high-emissivity groups is smaller than that from the low-emissivity groups. The minimum LST residual is 0.006 K (0.008 K) when the WVCs vary from 0 to 1.5 g/cm^2 and 1/cos(VZA) is equal to 1.0 for the high- (low-) emissivity group, and the maximum RMSE difference is 2.641 K (2.997 K) when the WVC ranges from 5 to 6.5 g/cm^2 and 1/cos(VZA) is equal to 2.0 for the high- (low-) emissivity group.

4) Overall Error on LST Retrieval: The overall error $(\delta(\text{LST}))$ on LST retrieval, which contains the instrument noises $(\delta(\text{LST}_{\text{NE}\Delta\text{T}}))$, the uncertainties of LSEs $(\delta(\text{LST}_\varepsilon))$ and WVCs $(\delta(\text{LST}_{\text{WVC}}))$, and the accuracy of the algorithm $(\delta(\text{LST}_r))$, can be expressed as follows:

$$\delta(\text{LST}) =$$
$$\sqrt{\delta^2(\text{LST}_r) + \delta^2(\text{LST}_{\text{NE}\Delta\text{T}}) + \delta^2(\text{LST}_\varepsilon) + \delta^2(\text{LST}_{\text{WVC}})}. \qquad (12)$$

The overall errors on LST retrieval for high-emissivity group and low-emissivity group are shown in Fig. 8 when the VZA is equal to 0°.

It can be seen that the maximum RMSE is approximately 1.81 K (1.95 K) for the high- (low-) emissivity group with the uncertainties of NEΔT: 0.2 K, LSE: 1%, and WVC: 20%

TABLE III
DIFFERENCE BETWEEN THE LST RETRIEVAL RMSE WITH 20% UNCERTAINTY OF WVC AND LST RETRIEVAL RMSE WITHOUT WVC ERROR

WVC / LSE	$1/\cos(VZA)$	[0, 1.5] g/cm²	[1, 2.5] g/cm²	[2, 3.5] g/cm²	[3, 4.5] g/cm²	[4, 5.5] g/cm²	[5, 6.5] g/cm²
High-emissivity group	1.0	0.006	0.155	0.176	0.217	0.331	0.988
	1.2	0.006	0.182	0.207	0.272	0.357	1.279
	1.4	0.007	0.211	0.236	0.323	0.378	1.593
	1.6	0.008	0.242	0.263	0.378	0.393	1.956
	1.8	0.009	0.272	0.289	0.424	0.403	2.300
	2.0	0.010	0.304	0.315	0.460	0.418	2.641
Low-emissivity group	1.0	0.008	0.222	0.236	0.256	0.447	1.280
	1.2	0.008	0.243	0.265	0.290	0.472	1.578
	1.4	0.009	0.267	0.292	0.324	0.488	1.902
	1.6	0.010	0.292	0.317	0.365	0.499	2.277
	1.8	0.010	0.317	0.341	0.400	0.503	2.638
	2.0	0.011	0.343	0.364	0.427	0.512	2.997

TABLE IV
INFORMATION OF THE SELECTED SITES

Site name	Latitude, Longitude	Date	Imaging time of IRS (UTC)	Imaging time of MODIS (UTC)
Wuhai	39°52′1″N, 106°38′2″E	2021/3/11	04:11:50	04:20
Geermu	36°25′30″N, 94°12′E	2021/1/27	05:01:31	04:40
Duhuang	40°9′36″N, 94°20′6″E	2021/1/19	05:03:43	05:30
		2021/3/09	05:01:44	04:35
Baotou	40°51′N, 109°36′E	2021/2/18	03:59:03	04:05
		2021/2/22	03:56:53	03:40
		2021/3/10	03:48:03	03:40

under the wet atmospheric conditions; the minimum RMSE is approximately 0.49 K (0.56 K) for the high- (low-) emissivity group with the uncertainties of NEΔT: 0.2 K, LSE: 1%, and WVC: 20% under the dry atmospheric conditions.

V. LST RETRIEVAL RESULT FROM HJ-2A/IRS DATA AND ITS VALIDATION

A. Results of LST Retrieval From HJ-2A/IRS Data

In this study, seven HJ-2A/IRS images are used to evaluate the LST obtained from a refined GSW algorithm. These seven images were taken from four different regions of Wuhai, Geermu, Dunhuang, and Baotou, with surfaces covered by vegetation, rock, soil, and urban. The imaging times and the central latitude and longitude of the study areas are given in Table IV, and the sample images in CH_B9 are displayed in Fig. 9. To obtain LSTs from the HJ-2A/IRS observations, some data processing should be carried out in advance. First, the radiation calibration should be executed according to the radiation calibration coefficients from the image head files to obtain the radiance values of the TIR channels. To retrieve LSE from (4) to (8), fast line-of-sight atmospheric analysis of spectral hypercubes atmospheric calibration should be carried out to obtain the NDVI and reflectance values. The European Centre for medium-range weather forecasts reanalysis v5 WVC
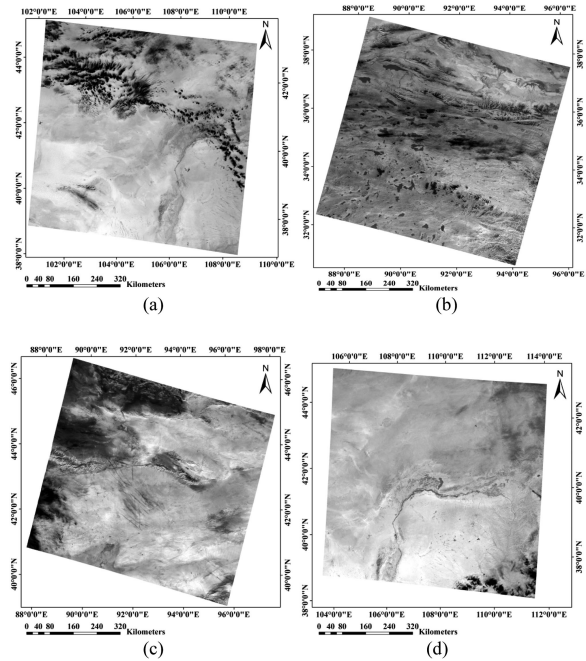

Fig. 9. Sample images of HJ-2A/IRS in CH_B9. (a) For Wuhai site in 2021/3/11. (b) For Geermu site in 2021/1/27. (c) For Dunhuang site in 2021/1/19. (d) For Baotou site in 2021/2/18.

dataset (which can be downloaded from)[1] is used to determine the algorithm coefficients in (3) according to the WVC values. Then, LSTs can be retrieved from (3) with knowledge of the LSE, TOA brightness temperature, and WVC.

B. Cross Validation

Due to the lack of *in situ* LST measurements, the MODIS LST product (MOD11_L2) is used to cross validate the LST obtained from HJ-2A/IRS TIR observations. The MOD11_L2 product provides LST and LSE values with a spatial resolution of 1 km. Because of the different projections between the MODIS LST product and HJ-2A/IRS images, the ENVI tool, called the MODIS conversion toolkit, is used to transform the projections. Additionally, the scientific dataset of quality control (QC) is

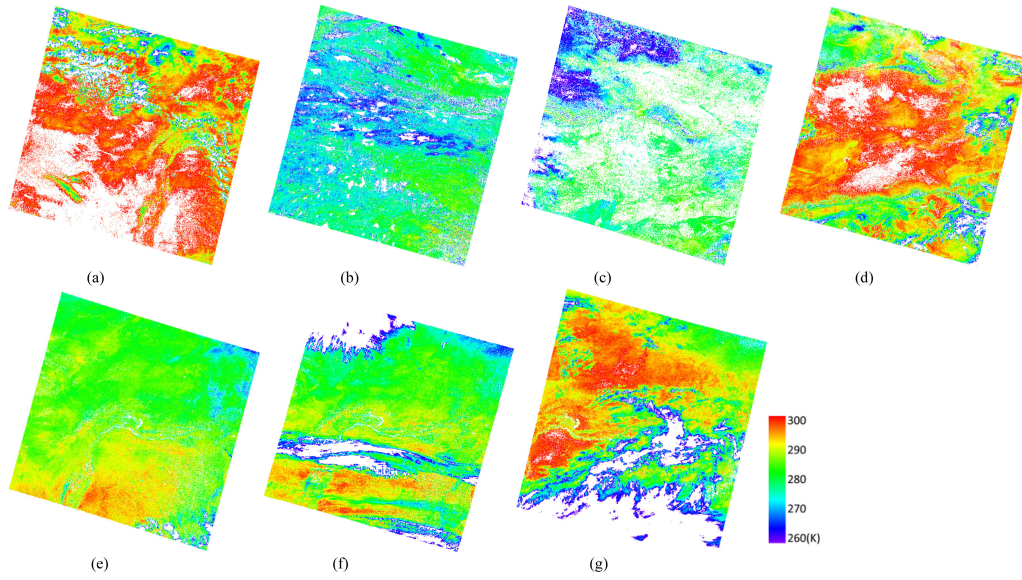[1]https://cds.climate.copernicus.eu/cdsapp#!/ search?type=dataset

Fig. 10. LST retrieved from the HJ-2A /IRS TIR observations. (a) For Wuhai site in 2021/3/11. (b) For Geermu site in 2021/1/27. (c) For Dunhuang site in 2021/1/19. (d) For Dunhuang site in 2021/3/09. (e) For Baotou site in 2021/2/18. (f) For Baotou site in 2021/2/22. (g) For Baotou site in 2021/3/10.
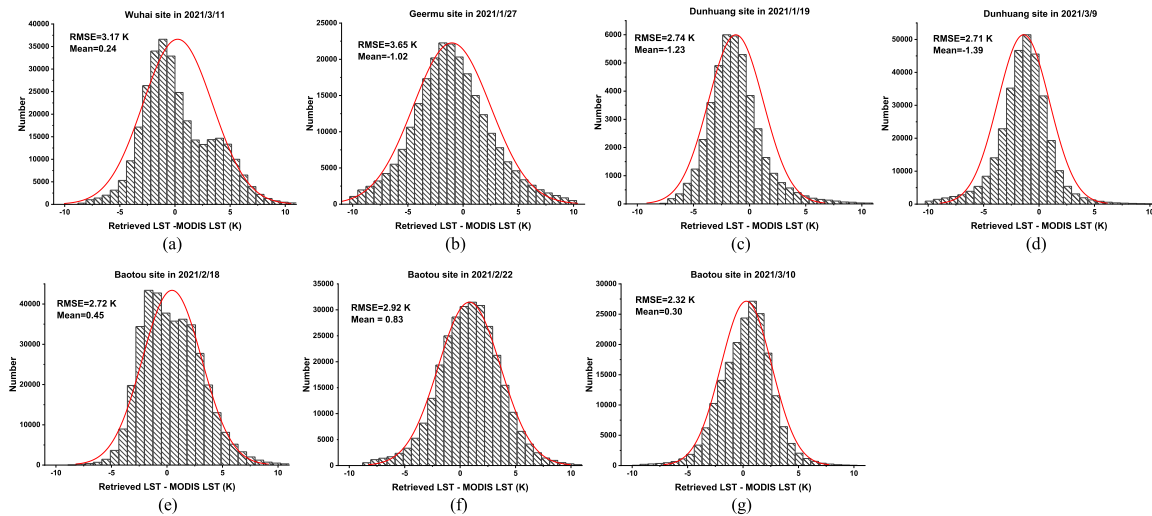

Fig. 11. Histogram and the envelope line of the difference between the retrieved LSTs from the HJ-2A/IRS TIR observations and the MODIS LST products. (a) For Wuhai site in 2021/3/11. (b) For Geermu site in 2021/1/27. (c) For Dunhuang site in 2021/1/19. (d) For Dunhuang site in 2021/3/09. (e) For Baotou site in 2021/2/18. (f) For Baotou site in 2021/2/22. (g) For Baotou site in 2021/3/10.

used to determine the usefulness of the MODIS pixel. The pixel is used only when the QC value is equal to 0 in this part.

The spatial resolutions of the MODIS LST products (spatial resolution: 1000 m) and LST retrieved from HJ-2A/IRS (spatial resolution: 96 m) are different, and the pixel aggregation algorithm, which can be expressed as (13), is used to put the two resolutions into the same resolution level [14]

$$\text{LST}_a = \sum_{i=1}^{N} \omega_i \text{LST}_i \bigg/ \sum_{j=1}^{N} \omega_j \qquad \text{with} \quad \omega_i = S_{i,p}/S_i \tag{13}$$

where LST_a is the LST after aggregation, ω_i is the weight of pixel i, N means there are N pixels in the target pixel, $S_{i,p}$ is the

partial area of pixel i overlapping with the target pixel, and S_i is the total area of pixel i.

Fig. 10 shows the LSTs retrieved from the HJ-2A TIR observations. Blue values refer to lower LSTs at approximately 260 K, red values represent higher LSTs at approximately 300 K, and white values represent the pixels covered by clouds. The LSTs in March [see Fig. 10(a), (d), and (g)] are obviously larger than those in January [see Fig. 10(b) and (c)]. For the same region [see Fig. 10(e) and (f)], the LST distribution of the two days with similar times (February 22 and February 18) is relatively consistent.

Fig. 11 shows the histograms with the difference between the retrieved LSTs from the HJ-2A/IRS TIR observations and the MODIS LST products. The RMSEs of the retrieved LSTs and

the MODIS LST products are between 2.3 and 3.7 K with a mean value of 2.89 K. It can be found that there are some differences between MODIS LST products and the retrieved LST retrieved from the HJ-2A/IRS TIR observations, the differences may be caused by the followings: the imaging time of MODIS and HJ-2A/IRS is different (see Table IV column 5), the difference is approximately 30 min, which may lead to different radiations for the two TIR images; or the upscaling processing for solving the different spatial resolutions between MODIS and IRS would produce errors for the cross validation.

VI. CONCLUSION

In this article, the nonlinear SW method was used to retrieve LSTs from HJ-2A/IRS TIR observations with a spatial resolution of 96 m. The algorithm coefficients were calculated from MODTRAN 5.0 using the statistical regression method under various atmospheric and surface conditions. For the purpose of improving the LST retrieval accuracy, the algorithm coefficients are calculated for different WVC subranges of [0, 1.5], [1, 2.5], [2, 3.5], [3, 4.5], [4, 5.5], and [5, 6.5] g/cm^2 and different LSE subranges of high- and low-emissivity groups. From the simulation analysis, the RMSEs are less than 2.4 K in the whole subrange and the RMSEs increase as the WVCs and VZAs increase. Moreover, the LST retrieval accuracies in the high-emissivity group are higher than those in the low-emissivity group. The minimum RMSE for the high-emissivity group (low-emissivity group) is 0.16 K (0.20 K) when the WVC belongs to [0–1.5] g/cm^2 and VZA equals 0°, while the maximum RMSE for the high-emissivity group (low-emissivity group) is 2.35 K (2.40 K) when the WVC varies from 5 to 6.5 g/cm^2 and VZA is equal to 60°.

The uncertainties of NEΔT, LSEs, and WVCs on LST retrieval are investigated in the sensitivity analysis. The analysis results show that, for the high- (low-) emissivity group, the maximum RMSE difference between the RMSE with NEΔT of 0.2 K and RMSE without NEΔT is 0.10 K (0.09 K) with WVC$\in$[0–1.5] g/cm^2 and VZA = 0°. For the high- (low-) emissivity group, 1% uncertainty of LSEs causes the LST retrieval errors varying from 0.88 (0.84) to 1.21 (1.19) K with a mean value of 1.05 (1.01) K when the atmospheres are dry, the errors varying from 0.19 (0.18) to 0.64 (0.62) K with a mean value of 0.42 (0.40) K under wet atmospheres. The minimum RMSE difference caused by uncertainty of 20% in the WVC is 0.006 K (0.008 K) when WVC ranges from 0 to1.5 g/cm^2 and 1/cos(VZA) equals 1.0 for the high- (low-) emissivity group, and the maximum RMSE difference caused by uncertainty of 20% in the WVC is 2.641 K (2.997 K) when WVC varies from 5 to 6.5 g/cm^2 and 1/cos(VZA) equals 2.0 for the high- (low-) emissivity group.

Finally, the MODIS LST products (MOD11_L2) are used to cross validate the retrieved LST because of the lack of ground measurement data. The results present that the RMSEs of the retrieved LSTs from the HJ-2A/IRS TIR observations and the MODIS LST products are between 2.3 and 3.7 K, with a mean value of 2.89 K.

REFERENCES

[1] S.-B. Duan *et al.*, "Validation of collection 6 MODIS land surface temperature product using *in situ* measurements," *Remote Sens. Environ.*, vol. 255, pp. 16–29, May 2019.

[2] X. Meng and J. Cheng, "Estimating land and sea surface temperature from cross-calibrated Chinese Gaofen-5 thermal infrared data using split-window algorithm," *IEEE Geosci. Remote Sens. Lett.*, vol. 17, no. 3, pp. 509–513, Mar. 2020.

[3] W. Li, L. Ni, Z.-L. Li, S.-B. Duan, and H. Wu, "Evaluation of machine learning algorithms in spatial downscaling of MODIS land surface temperature," *IEEE J. Sel. Topics Appl. Earth Observ. Remote Sens.*, vol. 12, no. 7, pp. 2299–2307, Jul. 2019.

[4] M. Lemus-Canovas, J. Martin-Vide, M. C. Moreno-Garcia, and J. A. Lopez-Bustins, "Estimating Barcelona's metropolitan daytime hot and cold poles using landsat-8 land surface temperature," *Sci. Total Environ.*, vol. 699, Jan. 2020, Art. no. 134307.

[5] W. Zhao, S.-B. Duan, A. Li, and G. Yin, "A practical method for reducing terrain effect on land surface temperature using random forest regression," *Remote Sens. Environ.*, vol. 221, pp. 635–649, Feb. 2019.

[6] E. Zhao, C. Gao, X. Jiang, and Z. Liu, "Land surface temperature retrieval from AMSR-E passive microwave data," *Opt. Express*, vol. 25, pp. A940–A952, Oct. 2017.

[7] C. B. Field, M. J. Behrenfeld, J. T. Randerson, and P. Falkowski, "Primary production of the biosphere: Integrating terrestrial and oceanic components," *Science*, vol. 281, no. 5374, pp. 237–240, Jul. 1998.

[8] J. Zhou *et al.*, "A thermal sampling depth correction method for land surface temperature estimation from satellite passive microwave observation over barren land," *IEEE Trans. Geosci. Remote Sens.*, vol. 55, no. 8, pp. 4743–4756, Aug. 2017.

[9] Y. Chen, S.-B. Duan, J. Labed, and Z.-L. Li, "Development of a split-window algorithm for estimating sea surface temperature from the Chinese Gaofen-5 data," *Int. J. Remote Sens.*, vol. 40, pp. 1621–1639, Aug. 2018.

[10] X. Ye, H. Ren, R. Liu, Q. Qin, Y. Liu, and J. Dong, "Land surface temperature estimate from Chinese Gaofen-5 satellite data using split-window algorithm," *IEEE Trans. Geosci. Remote Sens.*, vol. 55, no. 10, pp. 5877–5888, Oct. 2017.

[11] W. Zhao, H. Wu, G. Yin, and S.-B. Duan, "Normalization of the temporal effect on the MODIS land surface temperature product using random forest regression," *ISPRS J. Photogramm. Remote Sens.*, vol. 152, pp. 109–118, Jun. 2019.

[12] H. Ren, X. Ye, R. Liu, J. Dong, and Q. Qin, "Improving land surface temperature and emissivity retrieval from the Chinese Gaofen-5 satellite using a hybrid algorithm," *IEEE Trans. Geosci. Remote Sens.*, vol. 56, no. 2, pp. 1080–1090, Feb. 2018.

[13] X. Ye *et al.*, "Cross-calibration of Chinese Gaofen-5 thermal infrared images and its improvement on land surface temperature retrieval," *Int. J. Appl. Earth Observ. Geoinf.*, vol. 101, Sep. 2021, Art. no. 102357.

[14] E. Zhao, Q. Han, and C. Gao, "Surface temperature retrieval from Gaofen-5 observation and its validation," *IEEE Access*, vol. 9, pp. 9403–9410, Jan. 2021.

[15] B.-H. Tang, "Nonlinear split-window algorithms for estimating land and sea surface temperatures from simulated Chinese Gaofen-5 satellite data," *IEEE Trans. Geosci. Remote Sens.*, vol. 56, no. 11, pp. 6280–6289, Nov. 2018.

[16] J. Tan, T. Che, J. Wang, J. Liang, Y. Zhang, and Z. Ren, "Reconstruction of the daily MODIS land surface temperature product using the two-step improved similar pixels method," *Remote Sens.*, vol. 13, no. 9, Apr. 2021, Art. no. 1671.

[17] W. Zhao, J. He, Y. Wu, D. Xiong, F. Wen, and A. Li, "An analysis of land surface temperature trends in the Central Himalayan region based on MODIS products," *Remote Sens.*, vol. 11, no. 8, Apr. 2019, Art. no. 900.

[18] S. Westermann, M. Langer, and J. Boike, "Systematic bias of average winter-time land surface temperatures inferred from MODIS at a site on Svalbard, Norway," *Remote Sens. Environ.*, vol. 118, pp. 162–167, Mar. 2012.

[19] J. Kang, J. Tan, R. Jin, X. Li, and Y. Zhang, "Reconstruction of MODIS land surface temperature products based on multi-temporal information," *Remote Sens.*, vol. 10, no. 7, Jul. 2018, Art. no. 1112.

[20] K. Wang and S. Liang, "Evaluation of ASTER and MODIS land surface temperature and emissivity products using long-term surface longwave radiation observation at SURFRAD sites," *Remote Sens. Environ.*, vol. 113, no. 7, pp. 1556–1565, Mar. 2009.

[21] B. Song and K. Park, "Validation of ASTER surface temperature data with *in situ* measurements to evaluate heat islands in complex urban areas," *Adv. Meteorol.*, vol. 2014, 2014, Art. no. 620410.

[22] A. Barreto, M. Arbelo, P. A. Hernández-Leal, L. Núñez-Casillas, M. Mira, and C. Coll, "Evaluation of surface temperature and emissivity derived from ASTER data: A case study using ground-based measurements at a volcanic site," *J. Atmos. Ocean. Technol.*, vol. 27, no. 10, pp. 1677–1688, Oct. 2010.

[23] J. P. A. Martins *et al.*, "An all-weather land surface temperature product based on MSG/SEVIRI observations," *Remote Sens.,* vol. 11, no. 24, Dec. 2019, Art. no. 3044.

[24] A. Dumitrescu, M. Brabec, and S. Cheval, "Statistical gap-filling of SEVIRI land surface temperature," *Remote Sens.,* vol. 12, no. 9, Apr. 2020, Art. no. 1423.

[25] J. A. Sobrino, Y. Julien, J.-C. Jiménez-Muñoz, D. Skokovic, and G. Sòria, "Near real-time estimation of sea and land surface temperature for MSG SEVIRI sensors," *Int. J. Appl. Earth Observ. Geoinf.*, vol. 89, Jul. 2020, Art. no. 102096.

[26] J. C. Price, "Estimating surface temperatures from satellite thermal infrared data—A simple formulation for the atmospheric effect," *Remote Sens. Environ.*, vol. 13, no. 4, pp. 353–361, 1983.

[27] R. Niclos, V. Caselles, C. Coll, and E. Valor, "Determination of sea surface temperature at large observation angles using an angular and emissivity-dependent split-window equation," *Remote Sens. Environ.*, vol. 111, no. 1, pp. 107–121, Nov. 2007.

[28] L. Zhaoliang, M. P. Stoll, Z. Renhua, J. Li, and S. Zhongbo, "On the separate retrieval of soil and vegetation temperatures from ATSR data," *Sci. China Ser. D, Earth Sci.*, vol. 44, no. 2, pp. 97–111, Feb. 2001.

[29] L. M. McMillin, "Estimation of sea surface temperatures from two infrared window measurements with different absorption," *J. Geophys. Res.*, vol. 80, no. 36, pp. 5113–5117, 1975.

[30] Z. Wan and J. Dozier, "A generalized split-window algorithm for retrieving land-surface temperature from space," *IEEE Trans. Geosci. Remote Sens.*, vol. 34, no. 4, pp. 892–905, Jul. 1996.

[31] Z. Wan, "New refinements and validation of the MODIS land-surface temperature/emissivity products," *Remote Sens. Environ.*, vol. 112, no. 1, pp. 59–74, Jan. 2008.

[32] E. Zhao, Y. Qian, C. Gao, H. Huo, X. Jiang, and X. Kong, "Land surface temperature retrieval using airborne hyperspectral scanner daytime mid-infrared data," *Remote Sens.,* vol. 6, no. 12, pp. 12667–12685, Dec. 2014.

[33] Z.-L. Li *et al.*, "Satellite-derived land surface temperature: Current status and perspectives," *Remote Sens. Environ.*, vol. 131, pp. 14–37, Apr. 2013.

[34] Z.-L. Li *et al.*, "Land surface emissivity retrieval from satellite data," *Int. J. Remote Sens.*, vol. 34, no. 9/10, pp. 3084–3127, 2013.

[35] G.-M. Jiang, W. Zhou, and R. Liu, "Development of split-window algorithm for land surface temperature estimation from the VIRR/FY-3A measurements," *IEEE Geosci. Remote Sens. Lett.*, vol. 10, no. 4 pp. 952–956, Jul. 2013.

[36] M. R. Saradjian and Y. Jouybari-Moghaddam, "Land surface emissivity and temperature retrieval from landsat-8 satellite data using support vector regression and weighted least squares approach," *Remote Sens. Lett.*, vol. 10, no. 5, pp. 439–448, 2019.

[37] H. Tang and Z.-L. Li, "Land surface temperature retrieval from thermal infrared data," in *Quantitative Remote Sensing in Thermal Infrared: Theory and Applications*, 1st ed. New York, NY, USA: Springer, 2014, pp. 91–121.

[38] J. A. Sobrino *et al.*, "Land surface emissivity retrieval from different VNIR and TIR sensors," *IEEE Trans. Geosci. Remote Sens.*, vol. 46, no. 2, pp. 316–327, Feb. 2008.

[39] B.-H. Tang, K. Shao, Z.-L. Li, H. Wu, and R. Tang, "An improved NDVI-based threshold method for estimating land surface emissivity using MODIS satellite data," *Int. J. Remote Sens.*, vol. 36, no. 19/20, pp. 4864–4878, 2015.

[40] T. N. Carlson and D. A. Ripley, "On the relation between NDVI, fractional vegetation cover, and leaf area index," *Remote Sens. Environ.*, vol. 62, no. 3, pp. 241–252, Dec. 1997.

[41] J. A. Sobrino, N. Raissouni, and Z.-L. Li, "A comparative study of land surface emissivity retrieval from NOAA data," *Remote Sens. Environ.*, vol. 75, no. 2, pp. 256–266, Feb. 2001.

[42] J. Sobrino and M. Romaguera, "Land surface temperature retrieval from MSG1-SEVIRI data," *Remote Sens. Environ.*, vol. 92, no. 2, pp. 247–254, Aug. 2004.

[43] B.-H. Tang, K. Shao, Z.-L. Li, H. Wu, F. Nerry, and G. Zhou, "Estimation and validation of land surface temperatures from Chinese second-generation polar-orbit FY-3A VIRR data," *Remote Sens.,* vol. 7, no. 3, pp. 3250–3273, Mar. 2015.

[44] N. Wang, H. Wu, F. Nerry, C. Li, and Z.-L. Li, "Temperature and emissivity retrievals from hyperspectral thermal infrared data using linear spectral emissivity constraint," *IEEE Trans. Geosci. Remote Sens.*, vol. 49, no. 4, pp. 1291–1303, Apr. 2011.

[45] H. Ren *et al.*, "Atmospheric water vapor retrieval from Landsat 8 thermal infrared images," *J. Geophys. Res., Atmos.*, vol. 120, no. 5, pp. 1723–1738, Mar. 2015.

Enyu Zhao received the M.S. degree in signal and information processing from the Aerospace Information Research Institute, Chinese Academy of Sciences (CAS), Beijing, China, in 2013 and the Ph.D. degree in cartography and geographic information system from the College of Resources and Environment, University of Chinese Academy of Sciences, Beijing, China, in 2017. He was awarded by China Scholarship Council in 2014 as a joint Ph.D. student to study in the Engineering Science, Computer Science and Imaging Laboratory, University of Strasbourg, Strasbourg, France, for two years. He is currently an Associate Professor with the College of Information Science and Technology, Dalian Maritime University, Dalian, China. His research interests include quantitative remote sensing and hyperspectral image processing.
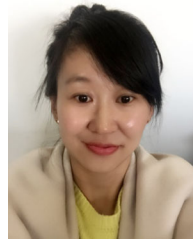
Caixia Gao received the B.S. degree in electronic and information engineering from the Xi'an University of Posts and Telecommunications, Xi'an, China, in 2006, the M.S. degree in computer science from the Academy of Opto-Electronics, Chinese Academy of Sciences, Beijing, China, in 2009, and the Ph.D. degree in cartography and geography information system from the University of Chinese Academy of Sciences, Beijing, China, in 2012.

She is currently an Associate Professor with Aerospace Information Research Institute, Chinese Academy of Sciences. Her research interests include in-orbit calibration and validation of optical sensors, and the retrieval of surface temperature and emissivity.

Qijin Han received the B.S. degree in mechanical and electronics engineering from Chang'an University, Xi'an, China, in 2007, and the M.S. degree in aircraft design from the China Academy of Space Technology, Beijing, China, in 2010.

He is currently an Associate Professor with the China Center for Resources Satellite Data and Application, Beijing, China. His research interests include radiometric calibration and validation of remote sensors, data processing, and quantitative applications of remotely sensed images.

Yuying Yao received the B.S. degree in communication engineering from Dalian Minzu University, Dalian, China, in 2019. She is currently working toward the master's degree in computer technology from Dalian Maritime University, Dalian, China.

Her research interests include quantitative remote sensing and hyperspectral image processing.

Yulei Wang (Member, IEEE) was born in Yantai, Shandong Province, China, in 1986. She received the B.S. and Ph.D. degrees in signal and information processing from Harbin Engineering University, Harbin, China, in 2009 and 2015, respectively.

She was awarded by China Scholarship Council in 2011 as a joint Ph.D. student to study in Remote Sensing Signal and Image Processing Laboratory, University of Maryland, Baltimore County, for two years. Since 2016, she has been with Dalian Maritime University, Dalian, China, where she is currently an Associate Professor with the Center for Hyperspectral Imaging in Remote Sensing, Information Science and Technology College. She was an Algorithm Engineer for advanced driver assistance systems with Beijing Jingwei Hirain Technologies Co., Inc. Her current research interests include hyperspectral image processing, vital signs signal processing, and recognition in vision systems of auto-driving.
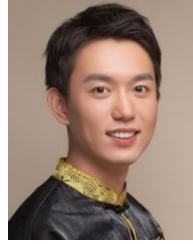
Haoyang Yu (Member, IEEE) received the B.S. degree in information and computing science from Northeastern University, Shenyang, China, in 2013, and the Ph.D. degree in cartography and geographic information system from the Key Laboratory of Digital Earth Science, Aerospace Information Research Institute, Chinese Academy of Sciences, Beijing, China, in 2019.

He is currently a Xing Hai Associate Professor with the Center of Hyperspectral Imaging in Remote Sensing, Information Science and Technology College, Dalian Maritime University, Dalian, China. His research focuses on models and algorithms for hyperspectral image processing, analysis, and applications.

Chunyan Yu (Member, IEEE) received the B.S. and Ph.D. degrees in environment engineering from Dalian Maritime University, Dalian, China, in 2004 and 2012, respectively.

From September 2014 to September 2015, she was a Visiting Scholar with the College of Physicians and Surgeons, Columbia University, New York, NY, USA. She is currently an Associate Professor with Information Science and Technology College, Dalian Maritime University. Her research interests include image segmentation, hyperspectral image classification, and pattern recognition.